Supplementary Materials

Detachable Soft Actuators with Tunable Stiffness Based on Wire Jamming

Long Bai, Hao Yan *, Jiafeng Li, Jiefeng Shan and Penghao Hou

School of Mechanical, Electronic and Control Engineering, Beijing Jiaotong University, Beijing 100044, China; 16116352@bjtu.edu.cn (L.B.); 18116014@bjtu.edu.cn (J.L.); 21121271@bjtu.edu.cn (J.S.); 20126009@bjtu.edu.cn (P.H.).
* Correspondence: hyan@bjtu.edu.cn

wire.

- Figure S13. Demonstration of a layer jamming structure with three different states.
- Figure S14. Comparison of the wire jamming structure with the layer jamming structure.
- Figure S15. Applied force versus deflection curves of kraft rope at 0 kPa.
- Figure S16. Spider plot with three different jamming structures.
- Figure S17. Bending stiffness experiments of single wire jamming structure.
- Figure S18. Applied force versus deflection curves for a wire jamming structure.
- Movie S1. Demonstration of experiment platforms, stiffness experiments, grasping process and soft glove.

Section S1. Theoretical model of fiber-reinforced soft actuator:

In this section, the theoretical model of a fiber-reinforced soft actuator is developed by a torque equilibrium equation, which focuses on the relationship between the positive air pressure and the bending angle under unloaded situations. First, when the actuator is in a bending state, we take the O point (blue color) in Figure S1a as the fulcrum. The relationship between the elastic moment M_r of silicone rubber and the bending torque M_p of internal air pressure can be expressed as:

$$M_p = M_r \tag{S1}$$

Figure S1b illustrates the rectangular cross-section of the soft actuator. The calculation of the bending torque of internal air pressure M_p can be expressed as:

$$M_p = \int_0^h w P_{in} (\alpha + b) d\alpha = whP_{in}(0.5h + b) \tag{S2}$$

where w is the width of the air chamber, b is the thickness from the bottom strain-limiting layer to the air chamber, h is the height of the air chamber and P_{in} is the positive air pressure. In order to obtain the tensile stresses of the silicone rubber, we introduce the Neo-Hookean model, as shown in Equation S3a. Then, Equation S3b can be obtained under the assumption that the silicone rubber is incompressible and the circumferential expansion of the actuator is neglected under fiber constraint. The final expression for the axial principal stress σ can be obtained by combining Equation S3a and Equation S3b.

$$W = \frac{\mu}{2}(I_1 - 3) \tag{S3a}$$

$$I_1 = \lambda^2 + \frac{1}{\lambda^2} + 1 \tag{S3b}$$

$$\sigma = \mu\left(\lambda - \frac{1}{\lambda^3}\right) \tag{S3c}$$

where I_1 is the first invariant of the three (axial, circumferential and radial) principle stretch ratios, λ is the axial principal stretch ratio and μ is the initial shear modulus. The elastic moment M_r is generated by the bending motion of the soft actuator. Therefore, the bending region can be divided into three parts: i) the bottom silicone rubber layer with the thickness b; ii) the lateral silicone rubber with wall thickness s; and iii) the top silicone rubber layer with thickness t. We assume that the curvature of the actuator is uniform during bending. The bending angle is θ and the bending radius of the strain-limiting layer is R. The axial principal stretch ratio λ_s of the soft actuator can be expressed in Equation S4, where the β is the local coordinate. Finally, the M_r can be obtained as follows:

$$\lambda_s = \frac{\beta + R}{R} = \frac{\theta\beta}{L} + 1 \tag{S4}$$

$$M_r = \int_0^b w \cdot L \cdot \beta \cdot \sigma_s \cdot d\beta$$
$$+2\int_0^{b+h+t} s \cdot L \cdot \beta \cdot \sigma_s \cdot d\beta \tag{S5}$$
$$+\int_{b+h}^{b+h+t} w \cdot L \cdot \beta \cdot \sigma_s \cdot d\beta$$

The theoretical equation of air pressure P_{in} and bending angle θ can be obtained by importing Equation S2 and Equation S5 into Equation S1.

$$P_{in} = \frac{M_r}{wh(0.5h+b)} \tag{S6}$$

Considering the applications of Figure 1a and Figure1b in the main text, we set the length L of the soft actuator to 105 mm and the width w to 15 mm. In order to prevent air leakage problems on the outer wall of the air chamber, the thickness b of the bottom silicone rubber layer is set to 3mm, the wall thickness s of lateral silicone rubber is set to 2.5 mm and the thickness t of the top silicone rubber layer is set to 3 mm. Therefore, the parameter μ of the silicone rubber and the height h of the air chamber are used as design variables in the design of the soft actuator. The relevant studies of silicone rubber are analyzed in detail in Section S2. It should be mentioned that the numerical simulation results deviate from the finite element simulation in Figure 1d and Figure S3, so we use k as a correction factor for the numerical solution. The numerical simulation results with the air chamber height h as the variable are shown in Figure S2. It is found that a higher air chamber h increases the bending angle under the same positive air pressure. However, the effect on the bending performance enhancement becomes weaker as the height of the air chamber h increases. In the end, we choose the actuator with a chamber height of 10 mm.

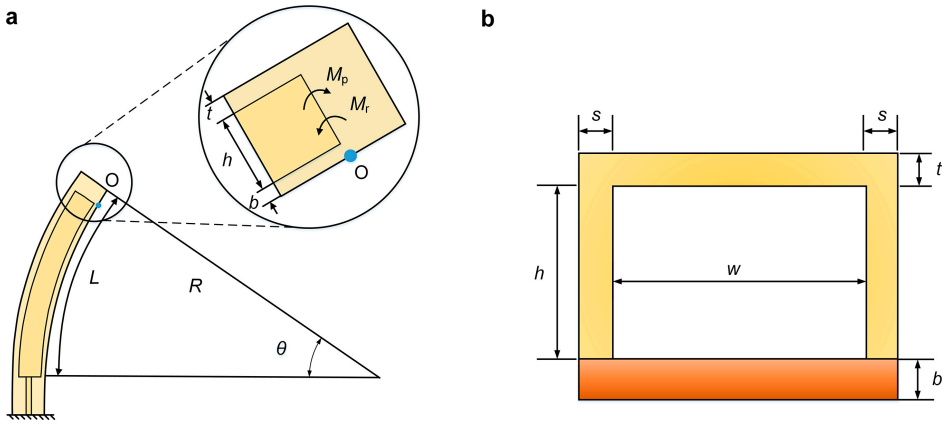

Figure S1. Illustration of a fiber-reinforced soft actuator in bending state. a) Side view of the soft actuator in bending state. Closeup view on the tip. b) Demonstration of the rectangular cross-section of the soft actuator.

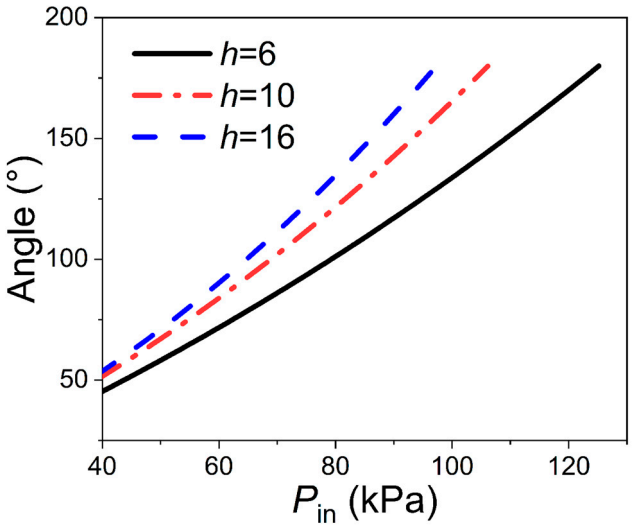

Figure S2. The influence of air chamber height *h* on bending angle.

Section S2. Uniaxial tensile test:

In order to obtain the mechanical properties of the silicone rubber (HC9010, Hengchang Liquid silicone plastic Corp., Guangdong, China), a uniaxial tensile test is conducted on a Microcomputer controlled universal testing machine (UTM4304, KASON, China). Figure S3a shows the detailed test procedure for the dumbbell-shaped silicone rubber samples, where the tensile speed is 500 mm/min. The average stress-strain curves are obtained for three different Shore hardness values (Figure S3b), where each test is repeated five times. The test results show that the tensile stress of the silicone rubber increases with the increase of the hardness value under the same strain. The hardness of the rubber also shows a positive correlation with Young's modulus. From the theoretical Equation S6 in Section S1, it can be concluded that the air pressure of the soft actuator is proportional to the initial shear modulus μ of the silicone rubber. In general, low hardness rubber has a small initial shear modulus μ. Therefore, the use of low-hardness rubber can effectively reduce the positive air pressure for actuation. In addition, low-hardness rubber has better shape adaptability and lower liquid viscosity.

Finally, we chose the silicone rubber with a Shore hardness of 10A. Figure S3c shows the fitting results of the Abaqus software (SIMULIA 2018, Dassault Systems, USA) to the hardness 10A. The results demonstrate that the Neo-Hookean model can describe the silicone rubber properties at small strains, while at larger strains, it is more appropriate to use the N=2 Ogden model. From the fitting results, the parameter C_{10} of Neo-Hookean can be obtained as 0.03975, and the initial shear modulus μ is further obtained as 0.0795 by the equation $\mu=2C_{10}$. It should be mentioned that the N=2 Ogden model is used for the finite element analysis in Figure 1d. Comparing the numerical simulation with the finite element simulation results, we can obtain the correction factor k for the bending angle as 1.25.

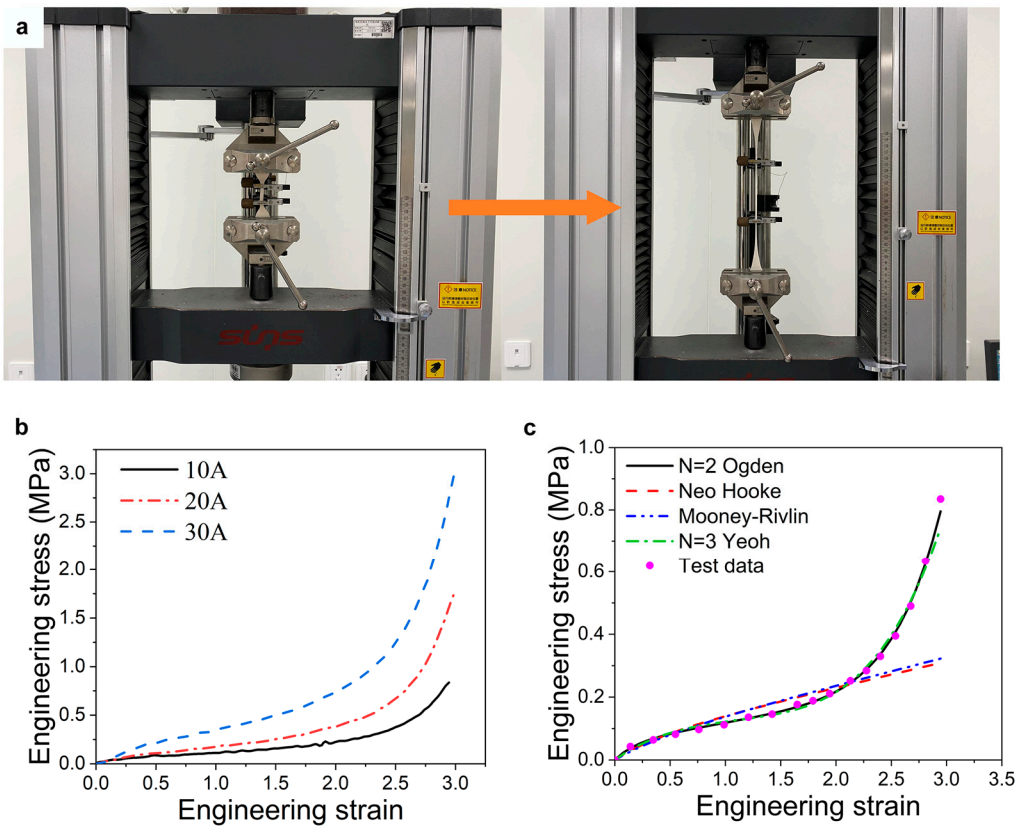

Figure S3. Uniaxial tensile test of the silicone rubber. a) Experimental setup for the dumbbell-shaped silicone rubber samples. b) Engineering stress versus engineering strain curves for silicone rubber samples with different hardness values (Shore hardness). Each curve is the average result of five repeat tests. c) Fitting results of different constitutive models.

Section S3. Installation layouts of tunable stiffness layer:

In this section, three candidate installation layouts are further analyzed. As shown in Figure 2a, layout 1 and layout 2 are the ideal installation options, commonly used in applications with granular jamming and laminar jamming structures. Our design concept is to minimize the effect of the tunable stiffness layer on the softness, elasticity and bending performance of the soft actuator before it works. First, we analyze the installation scheme of layout 1. The main advantage of the external installation scheme (i.e., layout 1) is that it avoids direct contact between the tunable stiffness layer and the target objects in applications and still maintains the flexibility of soft actuators. In addition, because the variable stiffness structure is wrapped with an airtight envelope, layout 1 avoids the issue of air leakage caused by touching sharp objects. Both installation schemes of layout 2 and layout 3 have contact problems. However, the advantage of layout 1 also brings the problem of the complicated fabrication process and challenging installation. The main text has introduced the stretching problem caused by the bending behavior, in which layout 1 is most affected by the bending angle, so the design of the variable stiffness layer needs to make two groups of staggered wires to avoid this problem. Two groups of wires are fixed at each end of the soft actuator. In addition, the choice of material and diameter is limited. Due to the sliding between wires, low stiffness or small diameter wires will lead to a severe localized arrangement. Moreover, the choice of the airtight envelope is also very important. The envelope of layout 1 needs to be a flexible silicone rubber film or an integrated design with a soft actuator to solve the stretching problem.

Second, we analyze the installation scheme of layout 2. As mentioned above, layout 2 presents problems mainly related to contact issues. However, layout 2 is not sensitive to bending behavior, so the structure design is relatively simple. There are three feasible ways to solve the contact problem as follows: i) using a puncture-resistant sealing film; ii) covering the outer side of the variable stiffness structure with a layer of silicone rubber; and iii) using an easily detachable assembly solution that can readily replace the failed functional layer. Therefore, we propose the use of puncture-resistant HDPE film (PEA001, Xinjinfeng Technology, Co. Ltd., Foshan, China) as a sealing membrane while applying Velcro strips to the detachable assembly scheme based on method 3. In the design of layout 2, we only need one group of wires as the jamming medium. This group of wires inside the sealing membrane

also does not need to be fixed at one end because the end of the jamming structure will be fixed with the end of the soft actuator in experiments or applications.

Third, we analyze the installation scheme of layout 3. In the study of variable stiffness, the lateral installation scheme (i.e., layout 3) is less used because of not only the contact problem but also the sensitivity to bending behavior. Since both sides of layout 3 can be installed with variable stiffness structures, layout 3 may have higher bending stiffness. Finally, based on the above analysis, it can be found that layout 2 does not cause severe compression or stretching after bending, and the internal structure design is the simplest. Therefore, layout 2 is a relatively good choice for the wire jamming design in this paper. It should be mentioned that for the comparison of the stiffness performance of the three layouts, further theoretical and experimental analysis is needed in future work.

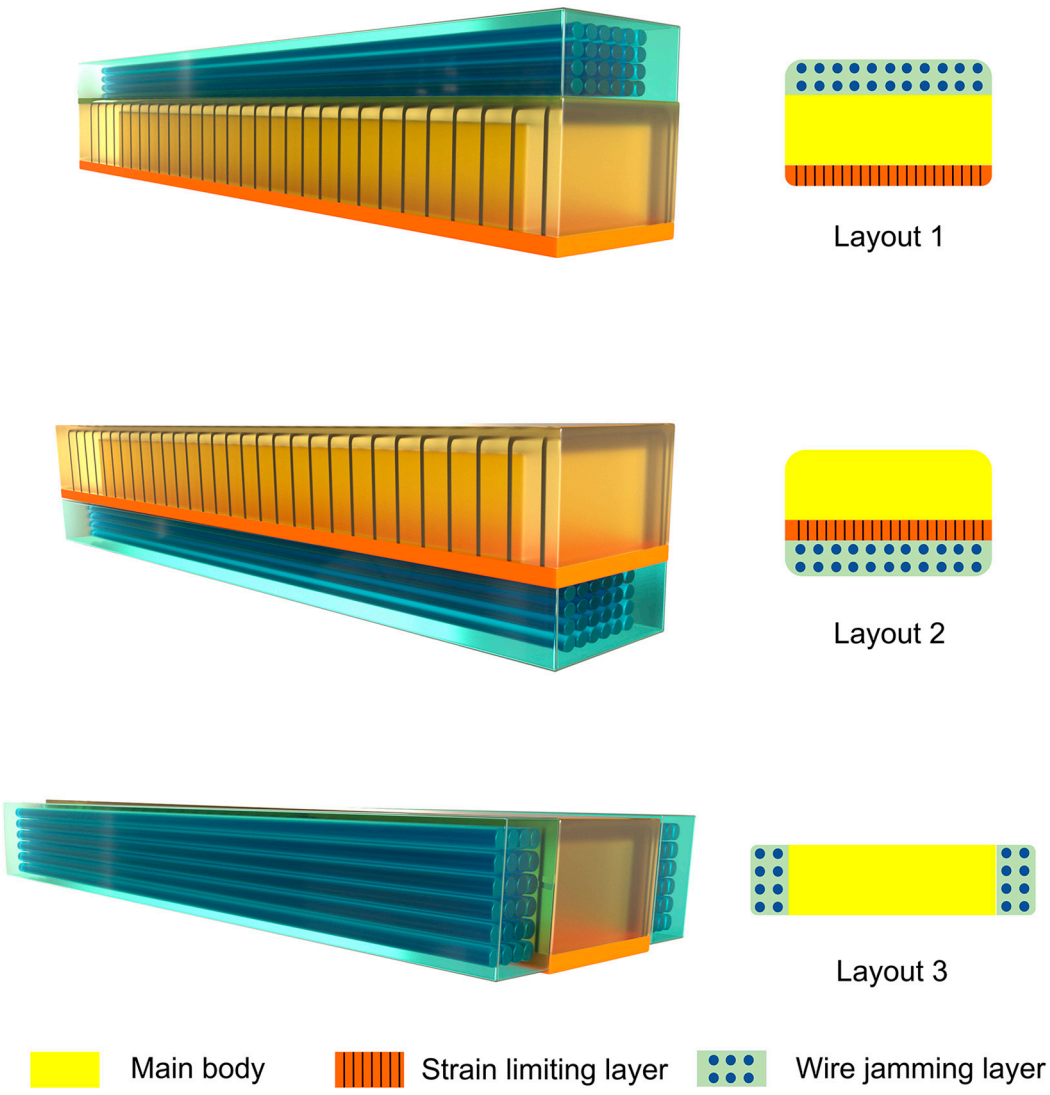

Figure S4. Demonstration of installation methods for wire jamming structure.

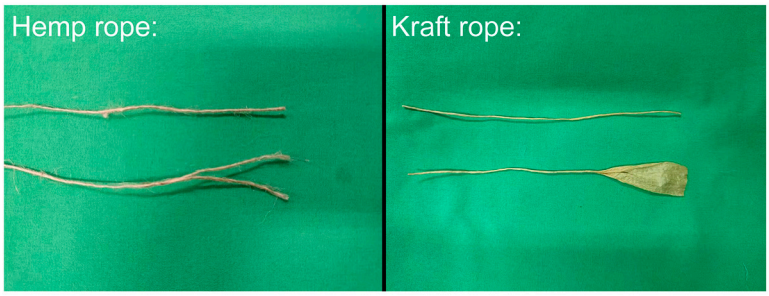

Figure S5. Demonstration of twisting methods. Hemp rope with two-strand twisted method (HQM07-06DD, Laizhou Huanqiu Rope Co. Ltd., China). Kraft rope with one-strand twisted method (HQB13-29, Laizhou Huanqiu Rope Co. Ltd., China).

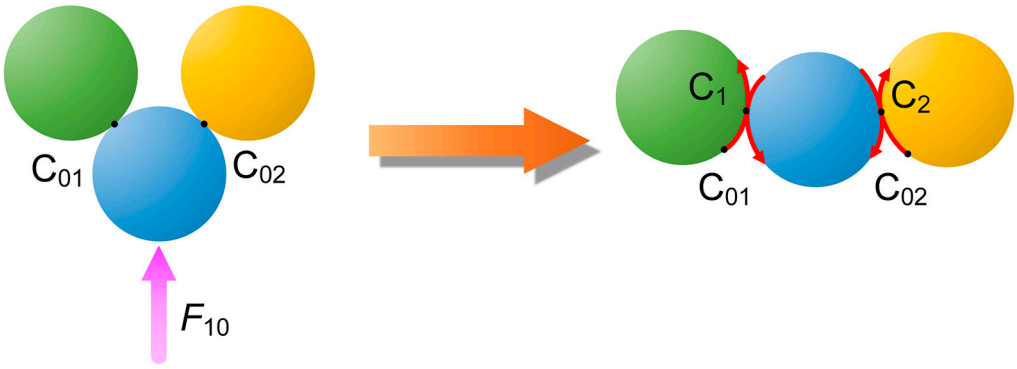

Figure S6. Localized rearrangement of wires in cross-section view, where C_{01} and C_{02} are original contact lines, C_1 and C_2 are final contact lines.

Section S4. Analytical model:

In this section, we further analyze the forces in the bending state. As we have already mentioned in the main text, it is assumed that these wires are in an independent state when the vacuum is off. According to the Euler-Bernoulli equation for a cantilever beam, the applied force F_e can be expressed as:

$$F_e = \frac{3\pi n_1 n_2 d_f^4 E}{64 a^3} v \tag{S7}$$

where n_1 and n_2 are the numbers of wires on the thickness and width, respectively. E is Young's modulus of the wires. d_f is the diameter of a single wire (Figure 2k). The wires enter the jammed state after the vacuum is on. Thus these wires are analyzed as a single beam. The beam thickness is $n_1 d_f$ and the width is $n_2 d_f$. The applied force F_r is expressed as:

$$F_r = \frac{n_2 n_1^3 d_f^4 E}{4 a^3} v \tag{S8}$$

In this paper, we use the ratio between the applied force to deflection as a quantitative indicator of stiffness. In Equation S7 and S8, the applied forces are related to the number of wires in the cross-section, the diameter of wires and the properties of the material at the same a with the same deflection v. We can also obtain a stiffness amplification factor k as follows:

$$k = \frac{F_r}{F_f} = \frac{16 n_1^2}{3\pi} \tag{S9}$$

From Equation S9, it can be found that the stiffness increases significantly with the increase of n_1. In the case of determining the wire diameter d_f (i.e., 1 mm), the parameter n_1 can also be expressed using the thickness $d = n_1 d_f$.

It should be mentioned that the calculation of the above equations is based on the assumption that there is no slip between the wires, so these equations are only applicable to the pre-slip phase (a small section of deflection before slip occurs) of the bending experiment. Under the above assumption, we still find a significant difference between the stiffness amplification factor calculated from the cantilever beam bending experiment and the result from Equation S9. We believe that the jamming structure will produce relative sliding when bending under a vacuum pressure of 0 kPa. The effect of friction will cause the result obtained from the calculation of Equation S7 to be much smaller than the experimental result, which leads to the theoretical calculation of Equation S9 with a larger stiffness amplification factor than the experimental result. Therefore, the prediction of the stiffness performance of the wire jamming structure using Equation S9 is limited, and only Equation S8 can be considered as a

relatively accurate expression. The theoretical model in this section can only be used as a design guide for the structural parameters and predict the bending stiffness before slip occurs.

In addition, the jamming structure in this paper is used in combination with a soft actuator, and in practice, the entire surface of the wire jamming structure is under stress (Figure S7). Therefore, further model improvements are needed in future studies.

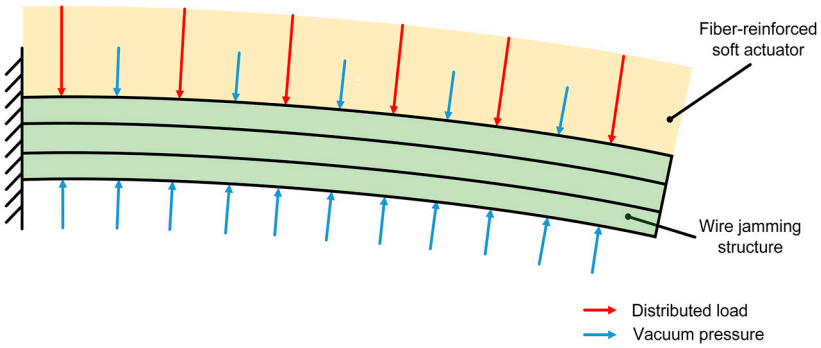

Figure S7. Schematic of a wire jamming structure under vacuum pressure and distributed load from the fiber-reinforced soft actuator.

Section S5. Geometric design parameters of wire jamming structure:

In this section, we detail the method of selecting the geometric parameters of the wire jamming structure and the number of wires. First, the variable stiffness soft actuator design is aimed at applications in robotic grippers and wearable devices, so a driving unit and a jamming unit are required. Our concept is to use the soft pneumatic actuator as the main structure and the jamming structure as the functional layer. Therefore, the geometric parameters of the jamming structure are determined by the dimensions and installation position of the soft actuator. The geometric parameters of the soft pneumatic actuator are described in Section S1 and the installation layout (i.e., layout 2) is analyzed in Section S3. Thus, the length of wires l_w is set to 150 mm, the total length of the airtight envelope is set to 160 mm and the width U of the cross-section is set to 15 mm. Finally, only the thickness d of the wire jamming structure is used as a variable to analyze the effect on bending stiffness. Obviously, the choice of thickness d is directly related to the number of wires. Figure S8 presents the detail of this relation, where d_f is the wire diameter and d_g is the gap between wires. We assume that the gap between wires is identical and that there is no gap between the membrane and wires. Equation S10 and Equation S11 can be achieved as follows:

$$d = n_1 d_f + (n_1 - 1) d_g \tag{S10}$$

$$U = n_2 d_f + (n_2 - 1) d_g \tag{S11}$$

Because the gap between wires cannot be measured precisely, we empirically choose 1 mm as the total value of gaps in a column or row during the fabrication process. Therefore, we can calculate the total number of wires to be filled inside after determining the width U and thickness d of the jamming structure. For example, when d=6 mm and U=15 mm, we can calculate a total of 70 wires are needed, where n_1=5, n_2=14.

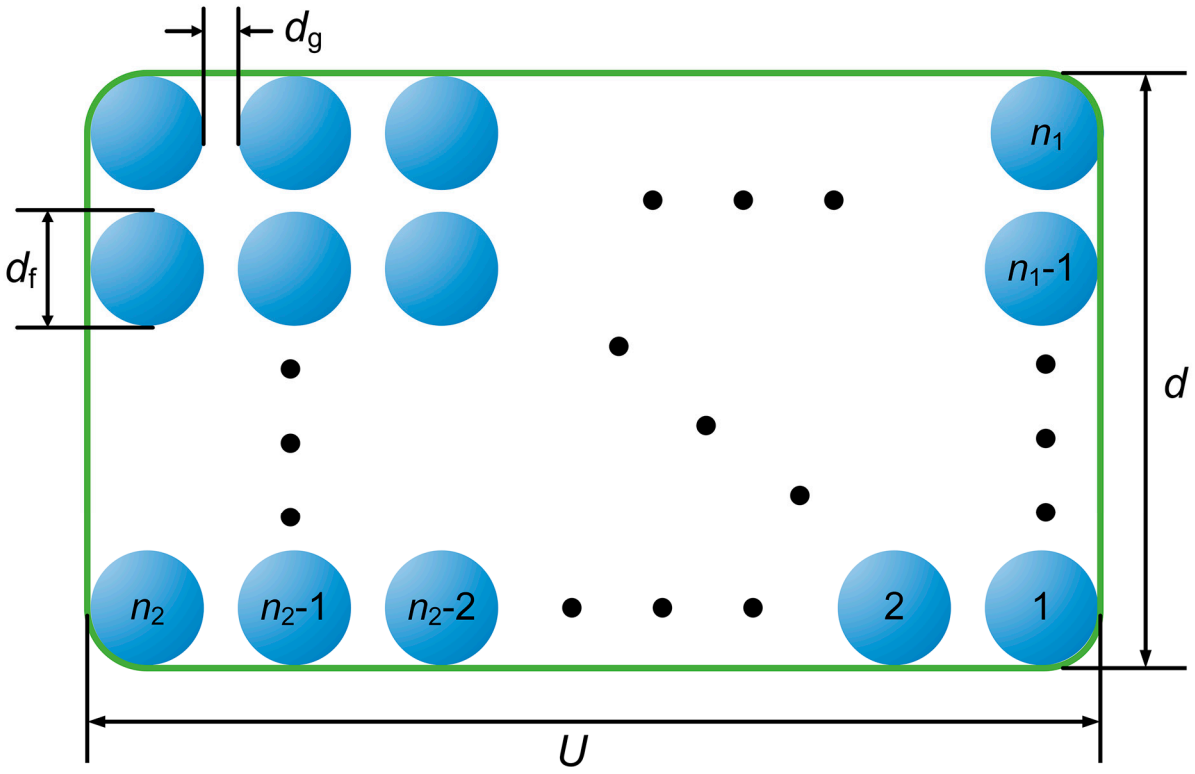

Figure S8. Illustration of wires on the cross-section of the jamming structure at a vacuum pressure is 0 kPa. The membrane is colored green, and the wires are colored blue.

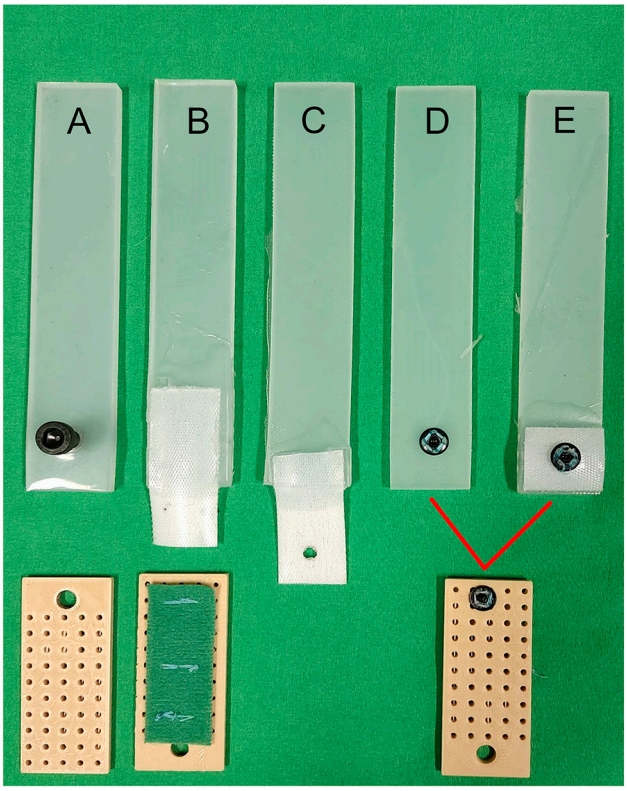

Figure S9. Comparative experiments of detachable solutions. There are five detachable solutions, each consisting of a silicone rubber strip, a fixing device and a connecting plate below it. Scheme A adopts the screw bolt and nut attaching method. Scheme B adopts the Velcro attaching method, where the silicone side is installed with double-sided Velcro (white color), and the connecting plate is installed with knitted loops Velcro. Scheme C adopts only double-sided Velcro. Scheme D and scheme E adopt the same snap fastener attaching method and the same connecting plate. The difference is that scheme E uses the double-sided Velcro as the middle layer for installing the snap fastener. It should be noted that the adhesive surface of the silicone rubber strip and the double-sided Velcro is the loop side.

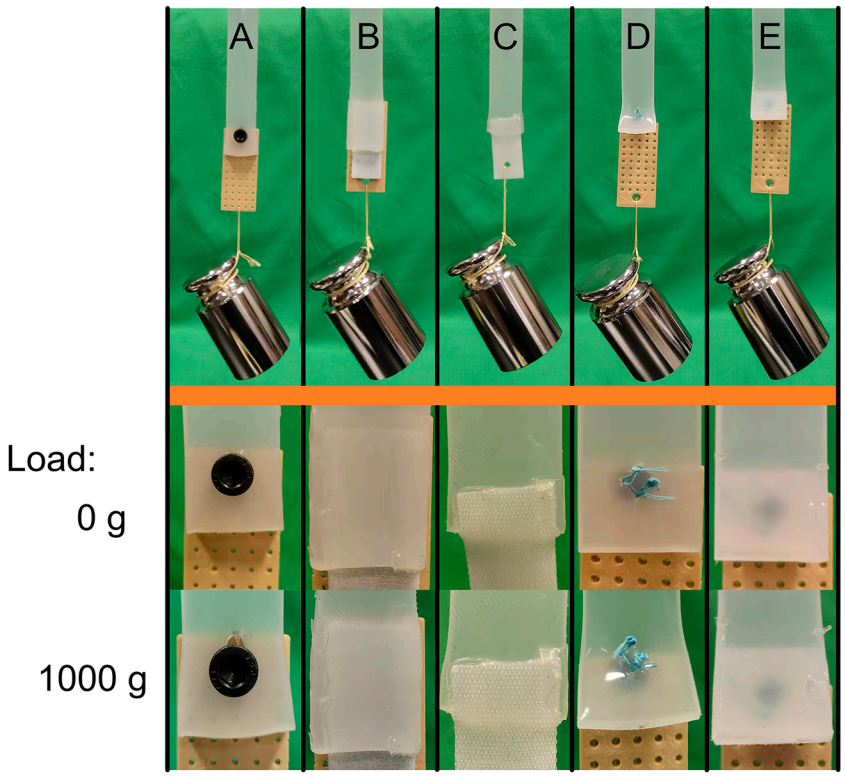

Figure S10. Experimental setup for detachable solutions. The five schemes are tested sequentially for 0g load and 1000g load tensile tests. A partially enlarged view is shown under the orange line in the figure. The experimental results show that scheme A and scheme D have the worst performance of attaching method. The rubber strips of scheme A and scheme D exhibit severe local tensile deformation after stretching. We also perform a 48-hour loading test for scheme A and scheme D. The rubber strips in both schemes show permanent tear damage. Scheme B and scheme E can be considered as two effective alternatives. Benefiting from the fact that the loop side of the Velcro strip can be firmly bonded to the rubber, there is no failure of the rubber in the attachment part. In addition, scheme C can also perform the tensile test well without using the connecting plate.

Section S6. Fabrication of the fiber-reinforced soft actuator:

In this section, the fabrication process of a fiber-reinforced soft actuator is described in detail. In order to solve the problem of complicated fabrication steps of the fiber-reinforced actuator and the difficulty of eliminating air bubbles, we have proposed a new fabrication scheme based on mold casting. The molds structures have been designed using Solidworks 2019 (Dassault Systems, USA), and then these molds are fabricated using 3D printing machines. The material used for the 3D printer is polylactic acid (PLA). The molding process can be divided into four steps (Figure S11). The first step is the fabrication of the inner silicone body. The two-component liquid silicone rubber is mixed well and vacuumed to remove air bubbles, and then the mixed liquid rubber is poured into the mold. Finally, the mold is placed in a 65 ℃ thermostat for 15 minutes to complete curing. The second step is to spiral-wrap the fibers along the length of the cured rubber in the first step. The main rubber body has pre-designed teeth grooves for guiding and fixing the fibers. It is important to note that the main body needs to be placed on the stick-like mold (orange color) before winding. The surface of the stick-like mold needs to be sprayed with a mold release agent (Ease Release 200, Smooth-On Inc., USA). The third step is to fabricate the outer rubber layer of the soft actuator. The function of the outer rubber layer is to prevent misalignment of fibers and prevent gas leakage from fibers. Same as the previous step, the mold needs to be sprayed with the release agent. Then, the new mold is poured with the mixed silicone liquid. Finally, the main body with wrapped fibers is turned over and pushed into the mold. The fourth step is to fabricate the strain-limiting layer. Unlike traditional soft actuators, for the first time in this paper, Velcro strips are proposed as the inextensible layer material. It is well known that Velcro is used across a wide array of industries and applications such as healthcare, the military and aircraft. Benefiting from a dense fiber surface, the loop side can robustly adhere to silicone rubber, such as Velcro strips have ever been used on the fixed end of a stretchable sensor. We use double-sided hook and loop fasteners as the final scheme, where the loop side (green color) is facing the air chamber of the soft actuator.

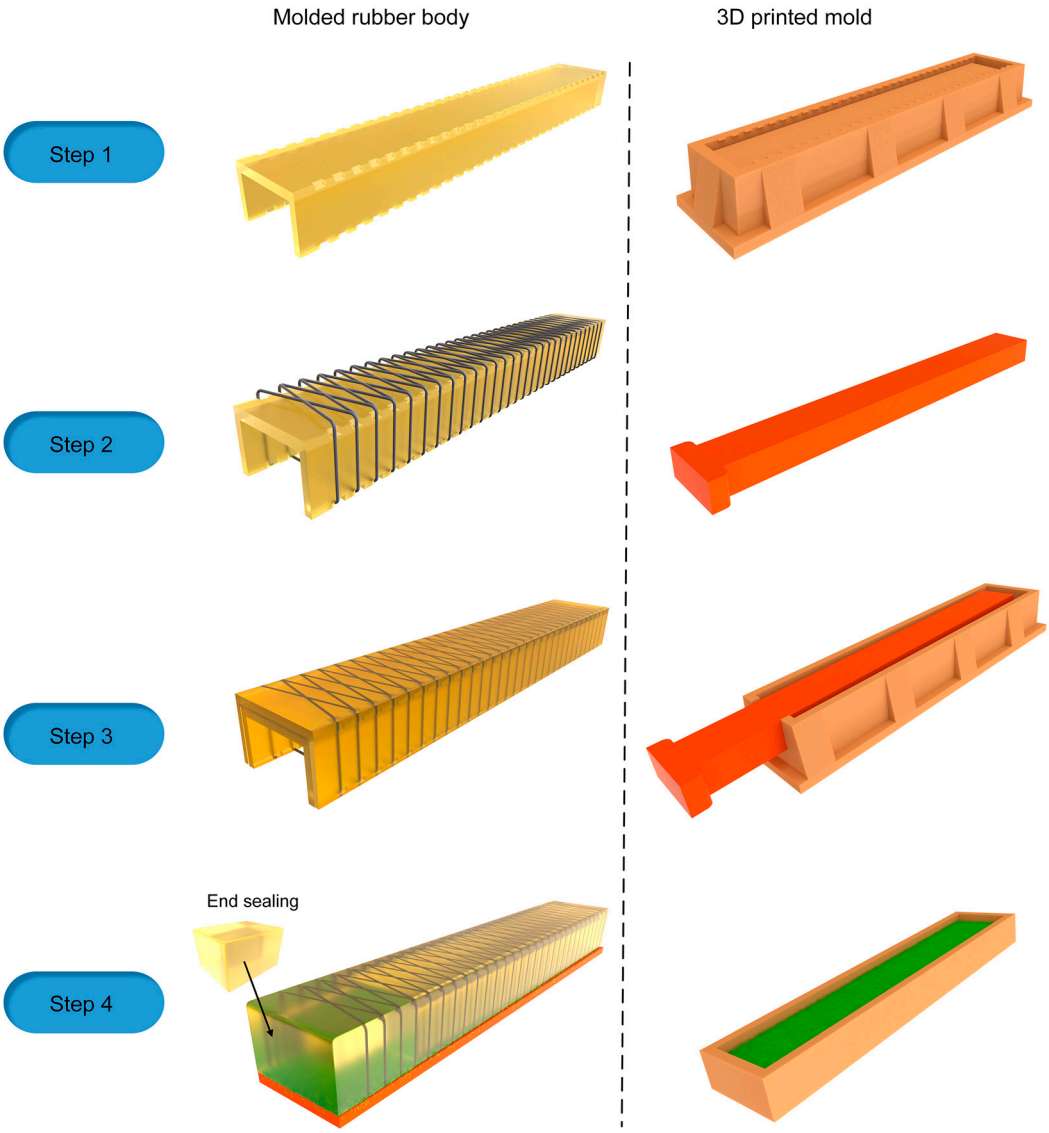

Figure S11. Fabrication process of the fiber-reinforced soft actuator.

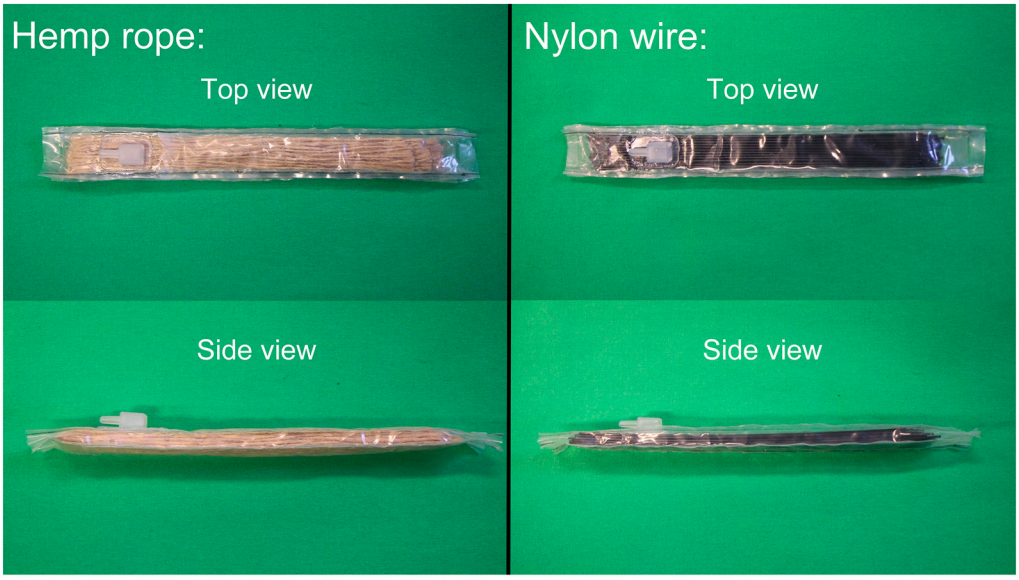

Figure S12. Demonstration of wire jamming structures made of hemp rope and nylon wire.

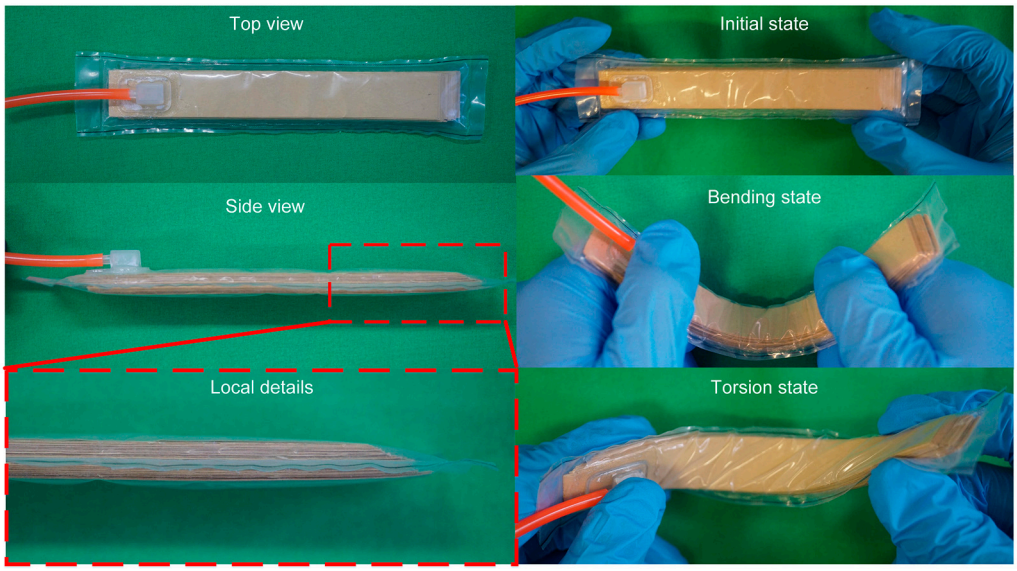

Figure S13. Demonstration of a layer jamming structure with three different states. The material used for layer jamming is kraft paper (Shibo Trading Co. Ltd., Guangzhou, China). The thickness of kraft paper is 0.1 mm.

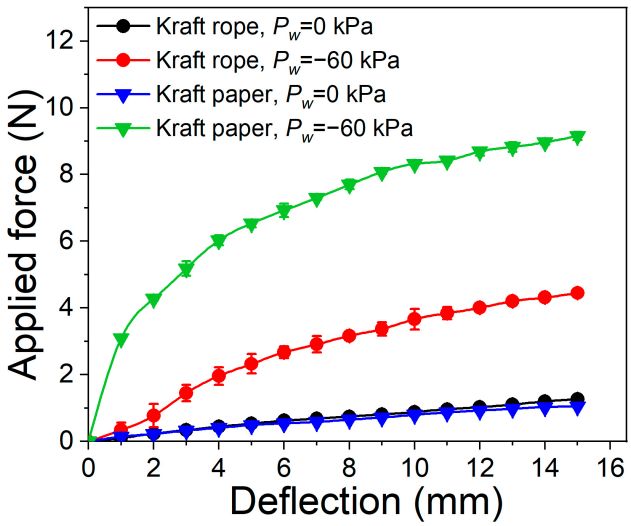

Figure S14. Comparison of the wire jamming structure with the layer jamming structure in the three-point bending experiment.

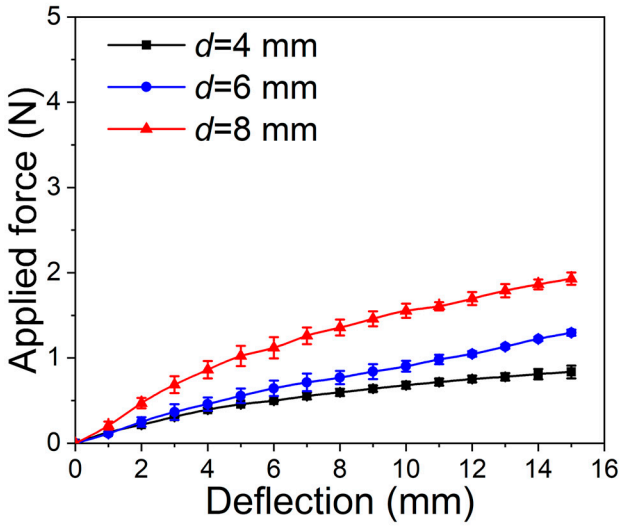

Figure S15. Applied force versus deflection curves of kraft rope under vacuum pressure of 0 kPa.

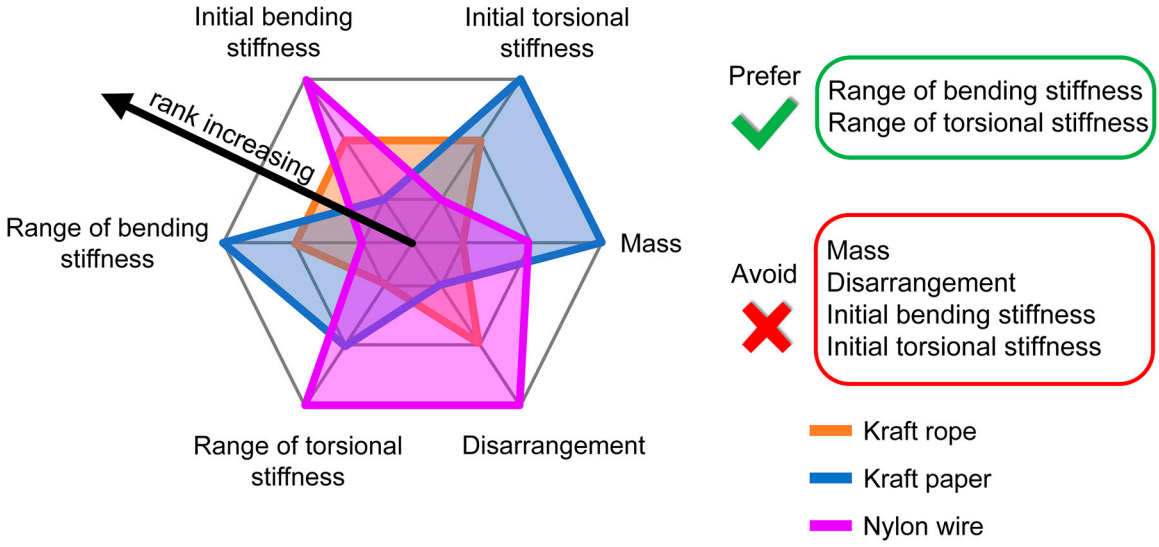

Figure S16. Spider plot with three different jamming structures. The three different jamming structures are the wire jamming structure using kraft rope, the layer jamming structure using kraft paper and the wire jamming structure using nylon wire. Six types of performance are used for comparative analysis. The ranking principle is based on the experimental data of bending and torsion in this paper. The content in the green box represents characteristics for which we want to have high values, while the content in the red box represents characteristics for which we want small values.

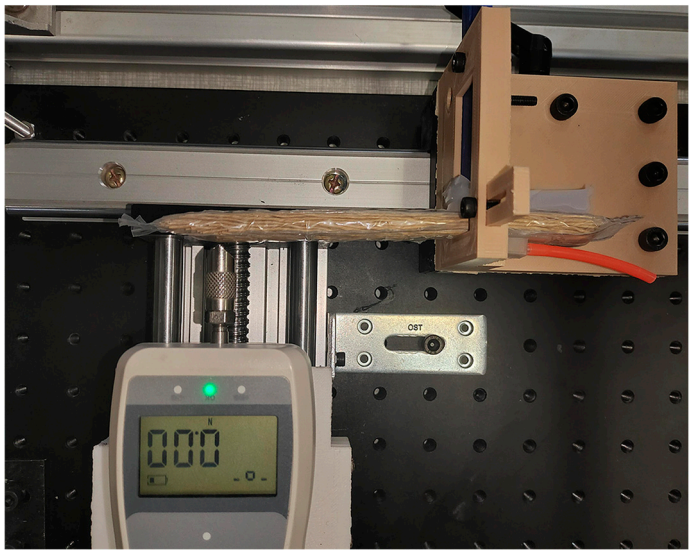

Figure S17. Bending stiffness experiments of single wire jamming structure.

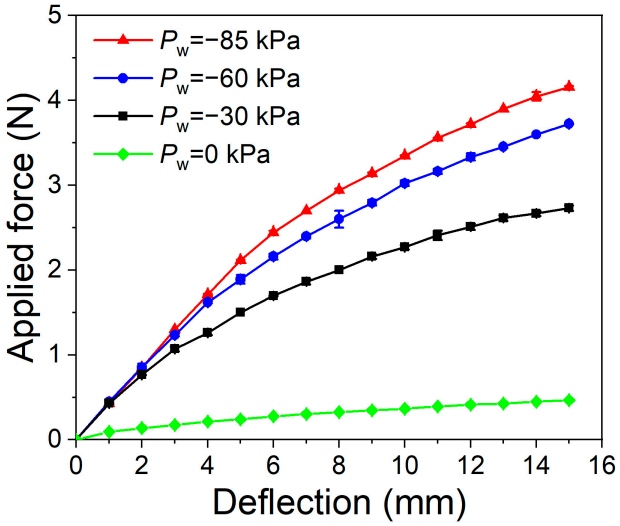

Figure S18. Applied force versus deflection curves from the bending stiffness experiments for a wire jamming structure with a thickness of 8 mm.